Multicomponent Distributed Acoustic Sensing

Ivan Lim Chen Ning & Paul Sava
Center for Wave Phenomena, Colorado School of Mines

ABSTRACT

Distributed Acoustic Sensing (DAS) data are increasingly used in geophysics. Being lower in cost and higher in spatial resolution makes DAS data appealing especially in boreholes where optical fibers are readily available. DAS has the potential to become a permanent reservoir monitoring tool with a reduced monitoring time interval. In order to accomplish this goal, the DAS data must contain enough information from different wave modes to characterize the reservoir. Thus far, however, the only usable DAS data is the axial strain measured by observing deformation along the fiber, but not multicomponent DAS data required to quantify different wave modes. We propose two approaches to obtain multicomponent DAS data by using either multiple parallel optical fibers, or a helical optical fiber. The multiple parallel optical fibers use the shape sensing method which is based on measurements of axial strain gradient to obtain the curvature of the optical cable and then reconstruct the components of the displacement. However, using the axial strain measurement in this optical fiber setup does not provide sufficient information to accurately reconstruct the displacements for different wave modes. The helical optical fiber makes use of the characteristics of the helix shape to obtain angle dependent strain measurements which provides sufficient information to reconstruct the strain tensor of the surrounding field.

Key words: distributed acoustic sensing, multicomponent, inversion

1 INTRODUCTION

Distributed Acoustic Sensing (DAS) is rapidly gaining popularity in the oil and gas industry especially for Vertical Seismic Profile (VSP) imaging and for reservoir monitoring (Mestayer et al., 2011; Cox et al., 2012; Mateeva et al., 2012, 2013; Daley et al., 2013; Madsen et al., 2013). The advantages of DAS for borehole applications in terms of costs, deployment mechanism and spatial resolution make its usage more attractive than conventional geophone acquisition (Lumens et al., 2013; Mateeva et al., 2013). The usage of optical fiber in wells is not an unfamiliar method as optical fiber has long been used for temperature measurement known as Distributed Temperature Sensing (DTS) (Hartog, 2000; Karaman et al., 1996).

DAS transforms an optical fiber into a distributed array of strain measuring tools. The acquisition requires an interrogator unit (IU) to send laser pulses into the optical fiber and detect back-scattered light from inhomogeneities along the fiber. The inhomogeneities are impurities caused either deliberately during manufacturing with the use of dopants or by manufacturing defects (Uzunoglu, 1981; Tsujikawa et al., 2005). The back-scattering generated by these inhomogeneities is called Rayleigh scattering. Analyzing the changes in amplitude and phase of the back-scattered light gives access to information such as strain and temperature.

As indicated by Lumens (2014), the DAS system is more sensitive in the axial direction compared to the radial direction, thus reducing the DAS measurable data to the axial strain which can be measured with acceptable signal-to-noise ratio. Where most of the DAS deployments are focused on borehole applications, multicomponent seismic data are desirable for the use in seismic characterization and monitoring (Davis et al., 2003; Stewart et al., 2003). To date, there is no published work that details mechanisms for extracting multicomponent data from the axial strain measurement using DAS. In order to acquire multicomponent data, alternative measuring devices are deployed such as geophones, which are costly and do not provide the dense spatial sampling of DAS. In this paper, we investigate possibilities to use different optical fiber configurations, in order to gain access to multicomponent information.

Our first approach is to use optical fiber as a shape sensing tool. The relationship between bending and difference in strain between two optical Fiber Bragg Gratings (FBG) has been discussed by Gander et al. (2000) as a curvature sensor. Flockhart et al. (2003) and Fender et al. (2006) demonstrate positive experimental results as a curvature sensor for structural monitor-

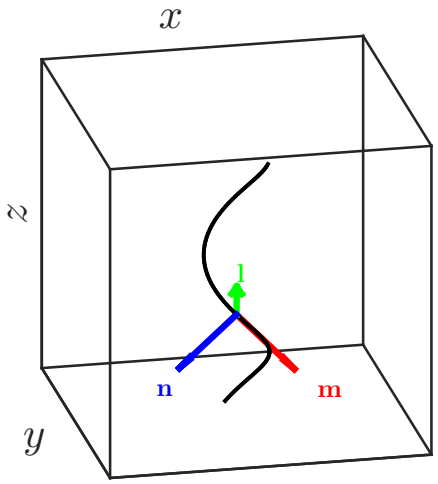


Figure 1. Optical fiber local coordinate. Vector $\boldsymbol{m}$ represents the axial direction of the optical fiber. Vectors $\boldsymbol{l}$ and $\boldsymbol{n}$ represent the two transverse orthogonal direction of the optical fiber.

ing. However, their discussion is limited to using the optical fiber as a shape monitoring tool, such as morphing-wing shape monitoring. In this paper, we exploit the shape sensing capabilities to obtain other data components that cannot be measured using a single optical fiber.

Our second approach is to use a helically shaped optical fiber. Using the characteristics of the helix and axial strain measurement of the optical fiber, we can calculate the entire strain tensor at every measuring location under the assumption that the seismic wavelength is much longer than the helix period. We show the theoretical relationship between the measured axial strain in the optical fiber and the full strain tensor in the surrounding area, and demonstrate the applicability of this strategy using a synthetic example.

This paper begins by reviewing the proposed approaches, followed by synthetic examples. While discussing the results, we also review the associated assumptions and limitations for both proposed approaches.

2 MULTIPLE PARALLEL OPTICAL FIBERS

The axial strain measurement by the optical fiber is a projection of the strain tensor from the surrounding area as a function of the optical fiber position. We introduce a local coordinate system of the optical fiber as illustrated in Figure 1, where $\mathbf{m}$ represents the direction along the optical fiber and, $\mathbf{l}$ and $\mathbf{n}$ represent transverse orthogonal directions. The relationship between the difference in axial strain $\Delta\varepsilon_{mm}$ and curvature κ is shown by Gander et al. (2000) as

$$\kappa = \frac{\Delta\varepsilon_{mm}}{r} \ , \tag{1}$$

where r is the distance between the two strain measurements. Consider an undisturbed system which consists of two optical fibers above and below the neutral axis, as shown in Figure 2(a). The top and bottom optical fibers have the same length dm, as no strain is applied. When the optical fibers undergo bending (Figure 2(b)), the length of the top and bottom optical fibers changes, thus creating a difference in axial strain ε_{mm} between them. The n-axis curvature for two horizontal optical fibers denoted with the superscript top and $bottom$ is

$$\kappa = \frac{\varepsilon_{mm}^{bottom} - \varepsilon_{mm}^{top}}{2\Delta n} \ . \tag{2}$$

We recognize that equation 2 effectively represents the centered finite-difference representation of the transverse derivative of the axial strain

$$\kappa = \frac{\varepsilon_{mm}(n+\Delta n) - \varepsilon_{mm}(n-\Delta n)}{2\Delta n} \approx \frac{\partial \varepsilon_{mm}}{\partial n} \ . \tag{3}$$

To obtain the second l-axis bend measurement in 3D, we require an additional optical fiber in the transverse direction which is either on the left or right of the top or $bottom$ optical fibers. We can further generalize to 3D the idea of curvature calculation by obtaining the axial strain gradient between optical fibers. Moore and Rogge (2012) show that the 2-axis bend measurement calculation can be obtained with an arbitrary circular arrangement. An example of the arrangement is shown in Figure 3(a) and the cross section of the arrangement is given in Figure 3(c). In the 2D illustration, the arrangement reduces to the original 2-axis bend measurement of Gander et al. (2000). The expression needed to calculate the local curvature vector for the respective optical fibers is (Moore and Rogge, 2012)

$$\boldsymbol{\kappa}_i = \frac{\varepsilon_{mm}^i}{2\Delta n}\left(cos(\theta_i)\hat{n} + sin(\theta_i)\hat{l}\right) \ , \tag{4}$$

where i is the optical fiber index, θ_i is the angle between the positive l-axis of the respective optical fiber as shown in Figure 3(c). Expression 4 transforms the scalar curvature into a vector curvature based on a specified reference axis, which in our case is the transverse axis along the fiber. The resultant curvature vector $\boldsymbol{\kappa}$ represents the overall bending of the optical fiber by summing all the curvature vectors of the respective optical fibers

$$\boldsymbol{\kappa} = \sum_{i=1}^{N} \boldsymbol{\kappa}_i \ . \tag{5}$$

Calculating the angle made by $\boldsymbol{\kappa}$ with respect to the reference axis gives

$$\varphi = \mathbf{tan^{-1}}\left(\frac{\kappa_{\mathbf{n}}}{\kappa_{\mathbf{l}}}\right) \ , \tag{6}$$

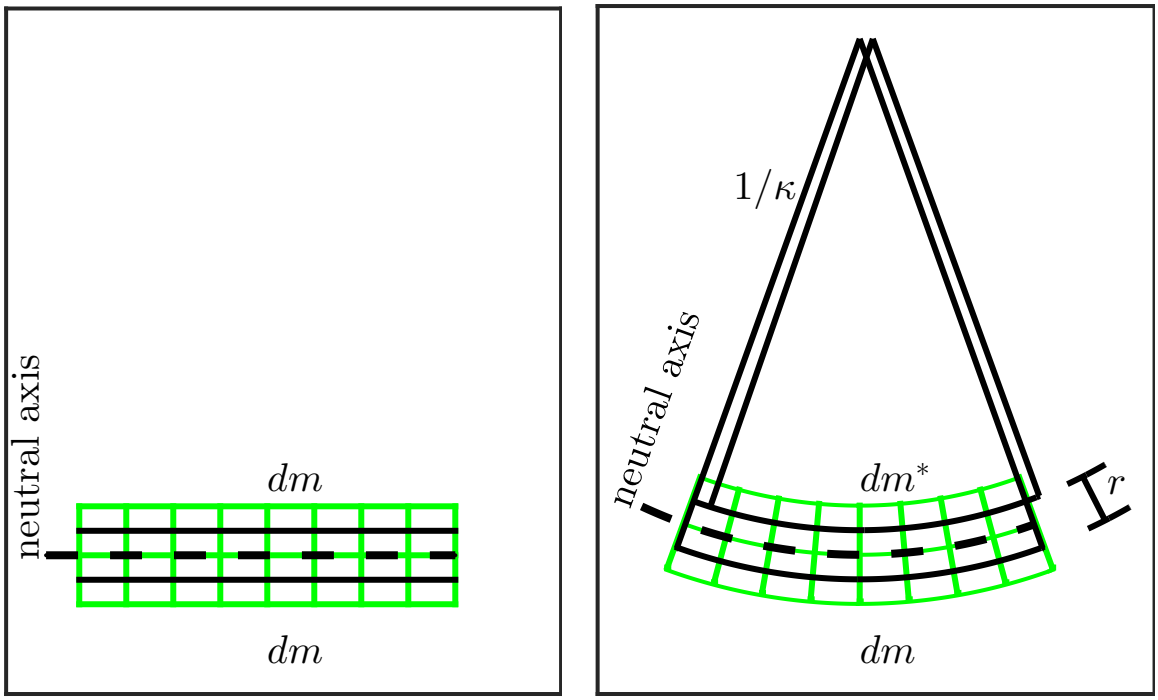
and from its derivative we can obtain the torsion of the optical fibers as

$$\tau = \frac{d\varphi}{dm} \ . \tag{7}$$

The curvature $\boldsymbol{\kappa}$, allows us to compute the displacement components through the geometrical definition

$$\boldsymbol{\kappa} = \frac{\partial^2 u_l}{\partial m^2}\hat{l} + \frac{\partial^2 u_n}{\partial m^2}\hat{n} \ . \tag{8}$$

An undisturbed optical fiber has no curvature, hence it records no displacement. A wavefield propagating through the



(a) (b)

Figure 2. Multiple parallel optical fibers bend diagram. Optical fiber (a) without bending and (b) with bending.

medium surrounding the optical fiber causes bending to the optical fiber, which is sensed as axial strain due to the curvature of the cable. Therefore, solving equation 8 using the calculated curvature yields the orthogonal displacement components (u_n and u_l) of the optical fiber depending on which curvature axis is used. The displacement along the fiber u_m can be obtained by integrating the measured axial strain ε_{mm} along the optical fiber. Therefore, we can obtain all the displacement components with respect to the local coordinate system of the optical fiber given that we have at least three parallel optical fibers.

2.1 Plane wave example

In order to understand how longitudinal (P) and shear (S) waves affect the optical fiber, we use a simple plane wave example to illustrate the particle movement around the optical fiber. In Figure 4(a), we show a plane wave propagating horizontally from left-to-right with the corresponding optical fiber movement in Figure 4(b). In this example, the particles on the optical fiber undergo compression and elongation in the wave propagation direction which is directly related to the measured axial strain ε_{mm} on the fiber as seen in Figure 5(a). Conversely, the particle motion of the S-wave is orthogonal to the wave propagation direction as shown in Figure 4(c) where the wave propagates vertically from top-to-bottom in this example. In this case the optical fiber does not sense any compressional motion, hence no measured axial strain is shown in Figure 5(b). The particle motion for the P- and S-waves are polarized in the same horizontal direction. Based on the results, the axial strain measures the elongation and compression deformation along the optical fiber.

We also consider the case of plane P- and S-waves impinging at an angle on the optical fiber to better understand the measures of axial strain. Figure 6(a) and 6(c) repeat the previous examples for P- and S-waves with a wave propagation incidence angle of 30° with respect to the vertical axis to observe the particle motion of the optical fiber. This example shows compression and elongation along the optical fiber for both P- and S-waves. The axial strain for P-wave in Figure 5(c) and S-wave in Figure 5(d) show that they share the same sign although they are different in terms of polarization, therefore both P- and S-waves share the same gradient. As the curvature measurement is ultimately the gradient of axial strain in the transverse direction, P- and S-waves have the same curvature to calculate the displacement u_n as shown in Figures 7(c) and 7(d). The consequence of the similar gradient of axial strain, we are unable to reconstruct the transverse displacement component with the correct sign for S-waves as illustrated by Figure 7(f) where the S-polarization is in the direction of P-polarization.

2.2 Discussion

Using the analytical plane waves example, we show that this arrangement lacks information to accurately reconstruct the displacement components using the calculated curvature for both P- and S-wave from axial strain measurements. In other words, the axial strain does not contain information about the

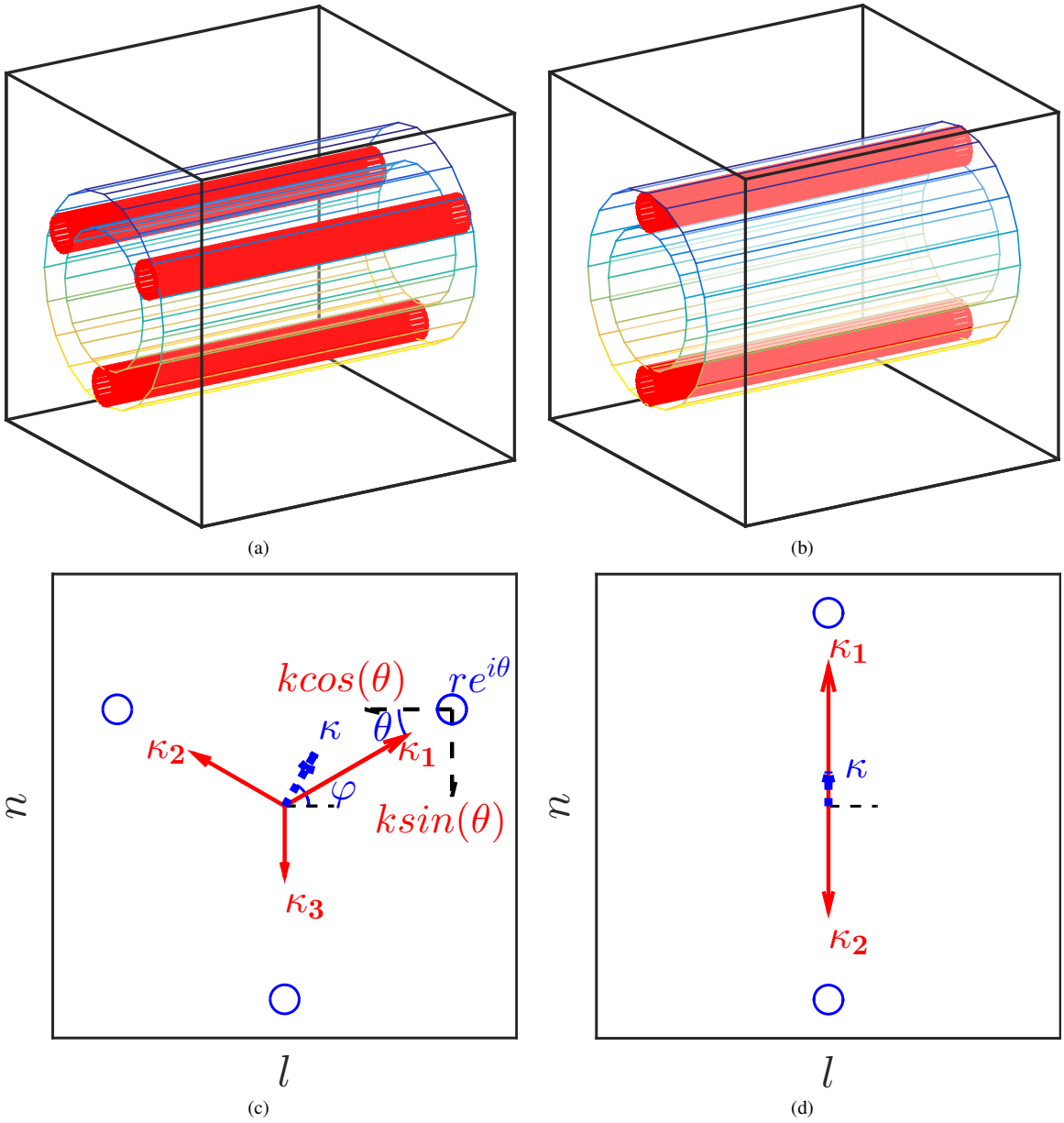


Figure 3. An example of the configuration for (a) three and (b) two optical fiber. The cross section of the cable with (c) three and (d)) two optical fiber core (circles) with respective curvature vectors (solid line). The resultant vector (dotted line) is the sum of the respective curvature vectors.

polarization vector to evaluate the polarization direction of different wave modes. This situation creates an ambiguity in reconstructing the displacement field.

As seen from our results, the calculated curvatures for P- and S-waves have the same sign which is a result of similar measured axial strain. The reconstructed displacement shares the same sign as the curvature. However, the analytical displacement results for P- and S-wave are opposite in sign. The disagreement between the curvature sign and the displacement for S-wave is not a result of an incorrect curvature calculation, but that of insufficient information to provide the reconstruct the displacement with the appropriate sign.

One of the main assumptions of this method is the fixed distance between the optical fibers. This is a crucial assumption as the distance between the optical fibers contributes towards the calculation of the curvature as a scaling factor. If the assumption is violated, the computed displacement from curvature no longer has the correct relative amplitude. In this method, we also assume that there is no twisting between the optical fibers. If twisting is present, the reference axis used to calculate the curvature changes and subsequently gives the

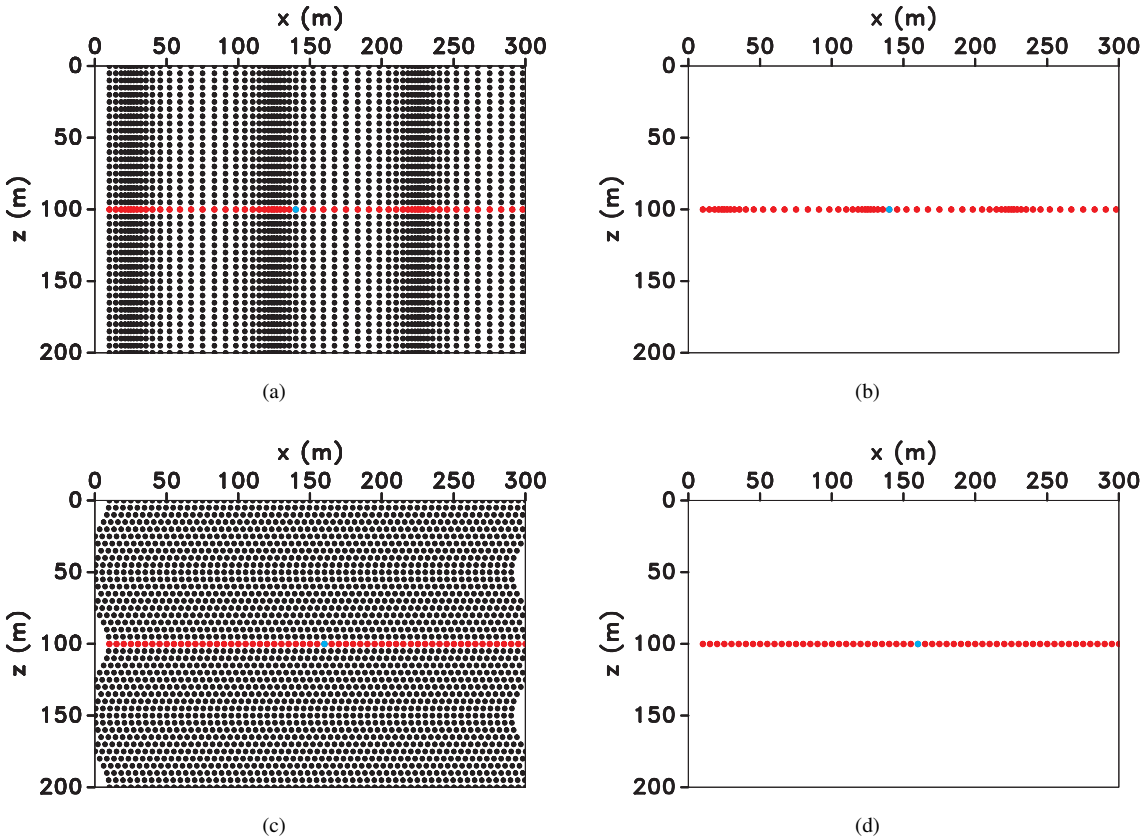


Figure 4. Particle motion for (a) a planar P-wave propagating with an incidence angle of 90° with respect to the vertical axis and (c) planar S-wave propagating with an incidence angle of 0° with respect to the vertical axis, together with the corresponding optical fiber displacement for (b) P-wave and (d) S-wave. The particle motion for both P- and S-waves is horizontal, but only the P-wave shows compression and elongation.

wrong curvature. However, the twisting can be tackled using torsion measurements prior to DAS data acquisition. The initial state of a twisted fiber gives a strain measurement that can be used to specify the torsion at the point of twist. Using the initial torsion, we can redefine the reference axis to correct the curvature calculation.

Based on the reconstructed displacement results, multiple parallel optical fibers do not give us enough information to accurately reconstruct the multicomponent DAS data. In the following section, we propose a different optical fiber layout that can provide adequate information for multicomponent DAS data reconstruction under certain assumption.

3 HELICAL OPTICAL FIBER

A helical optical fiber configuration for Distributed Acoustic Sensing (DAS) (Den et al., 2013) is designed to detect broadside acoustic signals, which refers to waves that arrive perpendicular to the direction along the optical fibre. Here, we exploit the helical shape as a tool to measure different projections of the strain field on to the optical fiber, i.e measure the projection of the surrounding strain tensor at a given location as a function of the angles made by the optical fiber with respect to the winding direction which is represented as a straight line in the middle of the optical fiber in Figure 8.

In this configuration, we make the assumption that the wavelength of the wavefield is much greater than the spatial wavelength of the helical optical fiber. This assumption is important so that we can group multiple measurements along the optical fiber to refer to the same strain tensor field. A larger wavelength of the wavefield gives us a slowly varying strain tensor field along a segment of the optical fiber which has a much smaller spatial wavelength. We approximate the slowly varying strain tensor field along the optical fiber segment to the same strain tensor field.

An example of helical optical fiber is shown in Figure 9(a), and its projection in 2D is shown in Figure 9(b). In Figure 9(c), we show the the angles with respect to the winding of the optical fiber in the z-axis as shown in Figure 9(a) and the azimuth for the location of measurement along the helical optical fiber. In 2D, Figure 9(d) shows the associate angle at for the location of measurement along the helical optical fiber.

The relationship between the axial strain measured by the optical fiber and the strain tensor of the surrounding area via

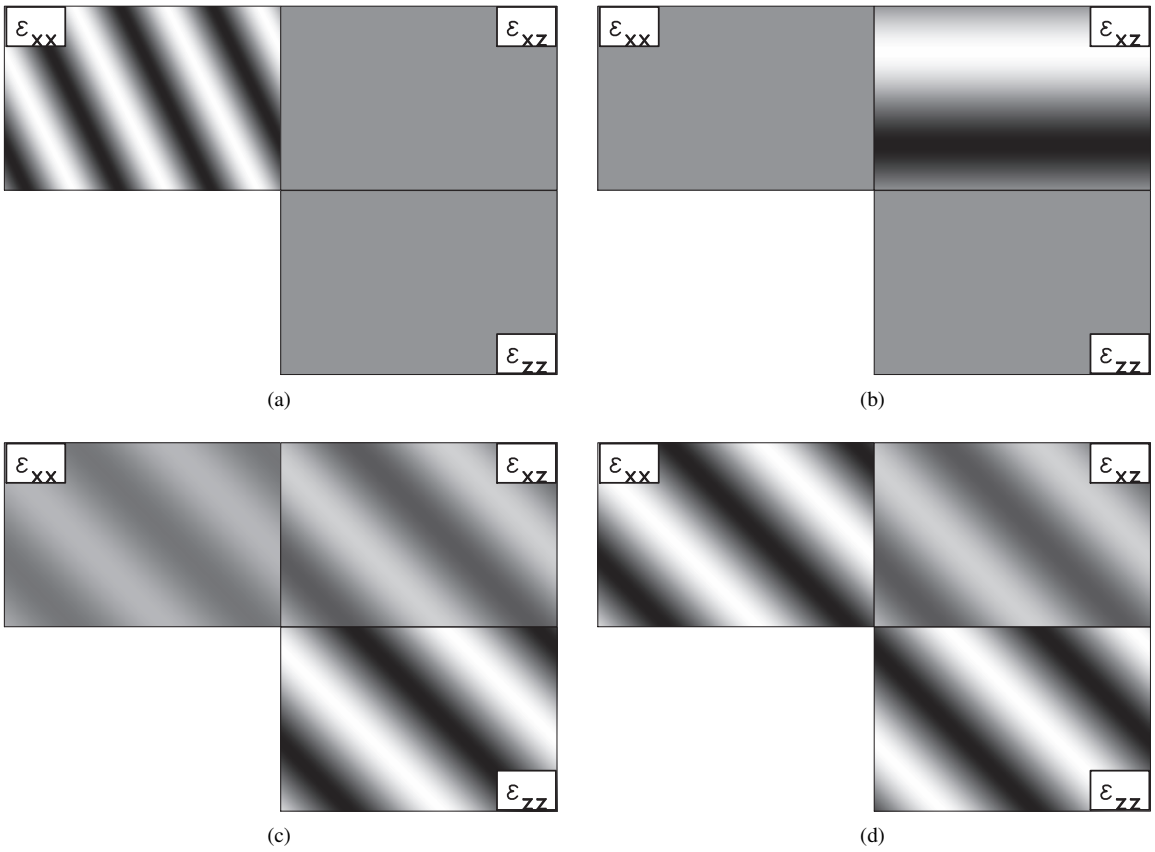


Figure 5. Strain tensor for (a) a plane P-wave propagating with an incidence angle of 90° with respect to the vertical axis, (b) a plane S-wave propagating with an incidence angle of 0° with respect to the vertical axis, and plane (c) P-wave and (d) S-wave propagating with an incidence angle of 30° with respect to the vertical axis. We can observe a measurable axial strain ε_{xx} for all the wavefields except for the plane S-wave propagation with an incident angle of 0° with respect to the vertical axis, which causes no compression and elongation, as seen in Figure 4(d). For each panel, the vertical axis is time and the horizontal axis is the receiver position.

the angles can be expressed through the strain tensor rotation relationship as (Young and Budynas, 2002)

$$\bar{\varepsilon} = \mathbf{R}\varepsilon\mathbf{R}^{\mathbf{T}} , \tag{9}$$

where the overline denotes the rotated strain tensor and $\mathbf{R}$ represents the rotation matrix. Rotation of a coordinate system can be written as

$$\begin{matrix} & \bar{\boldsymbol{\gamma}} & \\ \mathbf{m} & \mathbf{l} & \mathbf{n} \end{matrix}\begin{bmatrix} m_1 & l_1 & n_1 \\ m_2 & l_2 & n_2 \\ m_3 & l_3 & n_3 \end{bmatrix} = \begin{matrix} \\ \mathbf{R} \\ \\ \end{matrix}\begin{bmatrix} R_{11} & R_{12} & R_{13} \\ R_{21} & R_{22} & R_{23} \\ R_{31} & R_{32} & R_{33} \end{bmatrix}\begin{matrix} \\ \boldsymbol{\gamma} \\ \\ \end{matrix}\begin{bmatrix} 1 & 0 & 0 \\ 0 & 1 & 0 \\ 0 & 0 & 1 \end{bmatrix}\begin{matrix} \\ \\ \mathbf{x}\ \mathbf{y}\ \mathbf{z} \end{matrix} , \tag{10}$$

where $\bar{\boldsymbol{\gamma}}$ denotes axes of the rotated coordinate system ($\mathbf{m}$,$\mathbf{l}$,$\mathbf{n}$) and $\boldsymbol{\gamma}$ represents axes of the original coordinate system ($\mathbf{x}$,$\mathbf{y}$,$\mathbf{z}$). Therefore, the rotation matrix is represented by the local coordinate system of the optical fiber. Since the primary strain measurement of the optical fiber is due to axial strain only, we can narrow the problem to the rotated axial strain measurement in 3D at a location along the optical fiber as follows

$$\begin{matrix} \mathbf{d} \\ \\ \end{matrix}\begin{bmatrix} \varepsilon_{mm} \end{bmatrix} = \begin{matrix} \\ \mathbf{G} \\ \\ \end{matrix}\begin{bmatrix} R_{11}^2 & R_{12}^2 & R_{13}^2 & 2R_{11}R_{12} & 2R_{11}R_{13} & 2R_{12}R_{13} \end{bmatrix}\begin{matrix} \\ \mathbf{m} \\ \\ \end{matrix}\begin{bmatrix} \varepsilon_{xx} \\ \varepsilon_{yy} \\ \varepsilon_{zz} \\ \varepsilon_{xy} \\ \varepsilon_{xz} \\ \varepsilon_{yz} \end{bmatrix} , \tag{11}$$

where the observed data $\mathbf{d}$ vector represents axial strain measurements along a segment of the optical fiber which is assumed to be much smaller than the wavelength of the wavefield. The matrix $\mathbf{G}$ represents the expanded rotation matrix from equation 10. The number of rows in the data vector and matrix $\mathbf{G}$ refers to the number of measurements that we can assign to the same strain tensor of the surrounding area. Although in equation 11 we show only one measurements, in practice we use many more samples in our reconstruction.

Equation 11 can be solved using least-squares inversion where the kernel or forward operator $(\mathbf{G})$ is known. The data $(\mathbf{d})$ are the recorded axial strains along a segment of the helical

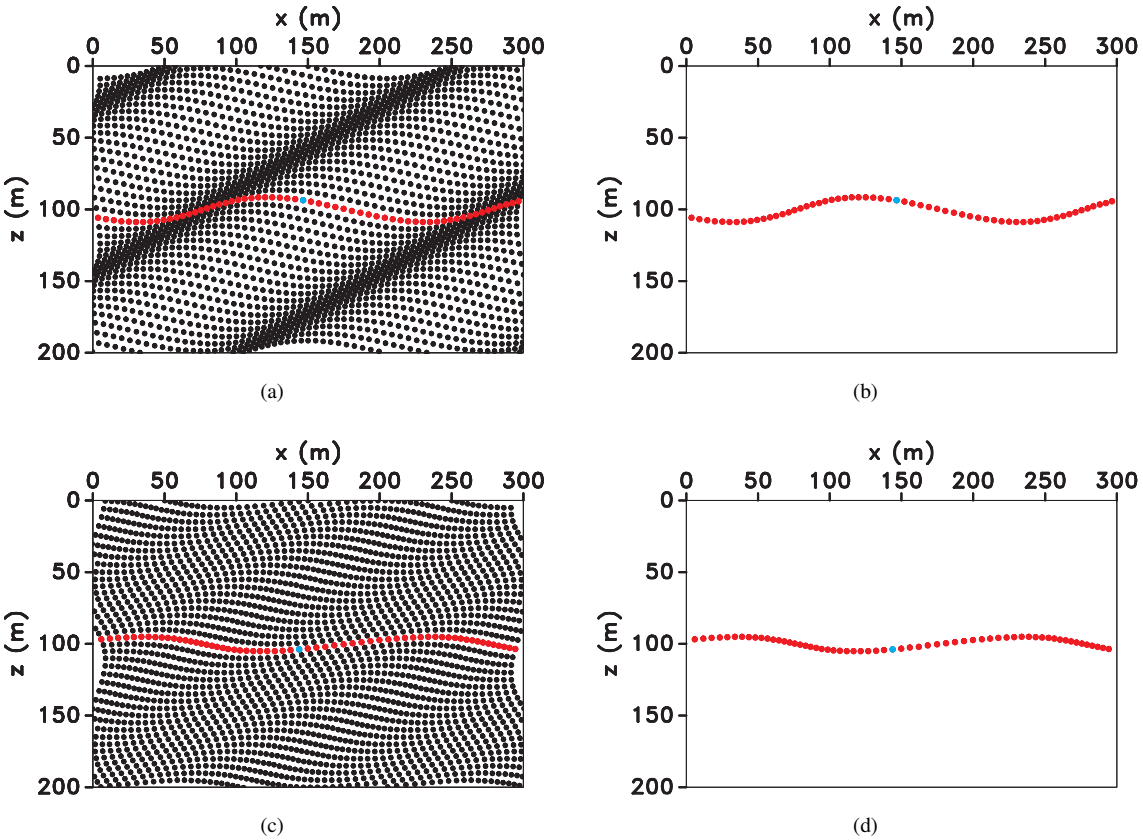


Figure 6. Particle motion for (a) a planar P-wave and (c) planar S-wave propagating with an incidence angle of 30° with respect to the vertical axis, together with the corresponding optical fiber displacement for (b) P-wave and (d) S-wave. Both P- and S-waves show compression and elongation.

optical fiber (this gives axial strain as a function of angles under the assumption that the seismic wavelength is much larger than the helix period holds) and the model $(\mathbf{m})$ is the strain tensor of the surrounding area. Minimizing the objective function

$$\mathcal{J} = \frac{1}{2}\|\mathbf{Gm} - \mathbf{d}\|^{\mathbf{2}} , \tag{12}$$

the model can be expressed as

$$\mathbf{m} = (\mathbf{G^T G})^{-\mathbf{1}}\mathbf{G^T d} . \tag{13}$$

The number of axial strain measurements with the associated angles can be varied accordingly with the parameters of the helix, such as the radius of the helix, the distance between the windings and the interval at which the measurements are made. In our example, the radius and the distance between the windings are much smaller than the wavelength of the wavefield. Figure 9(c) shows a 3D example with the associated angle and azimuth of the measured locations along the fiber. The 3D plot shows a constant measuring angle due to the characteristic of the helix with a constant wrapping angle, thus this configuration cannot provide a diverse set of angle dependent measurement to determine the strain tensor of the surrounding area. Using the same parameters, Figure 9(d) show a 2D example of the range of measurable angle dependent axial strain.

By introducing a varying winding distance along the fiber as shown in Figure 10(a), we obtain a better coverage for the measured angle dependent axial strain. This alternative configuration in 2D represents a chirp function as shown in Figure 10(b). Using the chirping helix measurements, we can solve equation 13 to obtain the strain tensor of the surrounding area.

3.1 Plane wave example

Assuming that the seismic wavelength is much larger than the helix period, we are able to measure axial strain $\varepsilon_{mm}(\theta)$ as a function of angle. The strain tensors of P- and S-waves are different as shown in Figure 11(a) and 11(c) where the horizontal axis is the measuring points along the optical fiber and vertical axis represents time. Therefore, the measured axial strain as a function of angles for P- and S-waves are different due to the contribution of all the elements in the strain tensor as expressed in equation 11. An example of a rotated strain field at a specific time for all angles is shown in Figure 12(a) for P-wave and Figure 12(b) for S-wave that illustrates the difference between the wave modes. By using the observed rotated

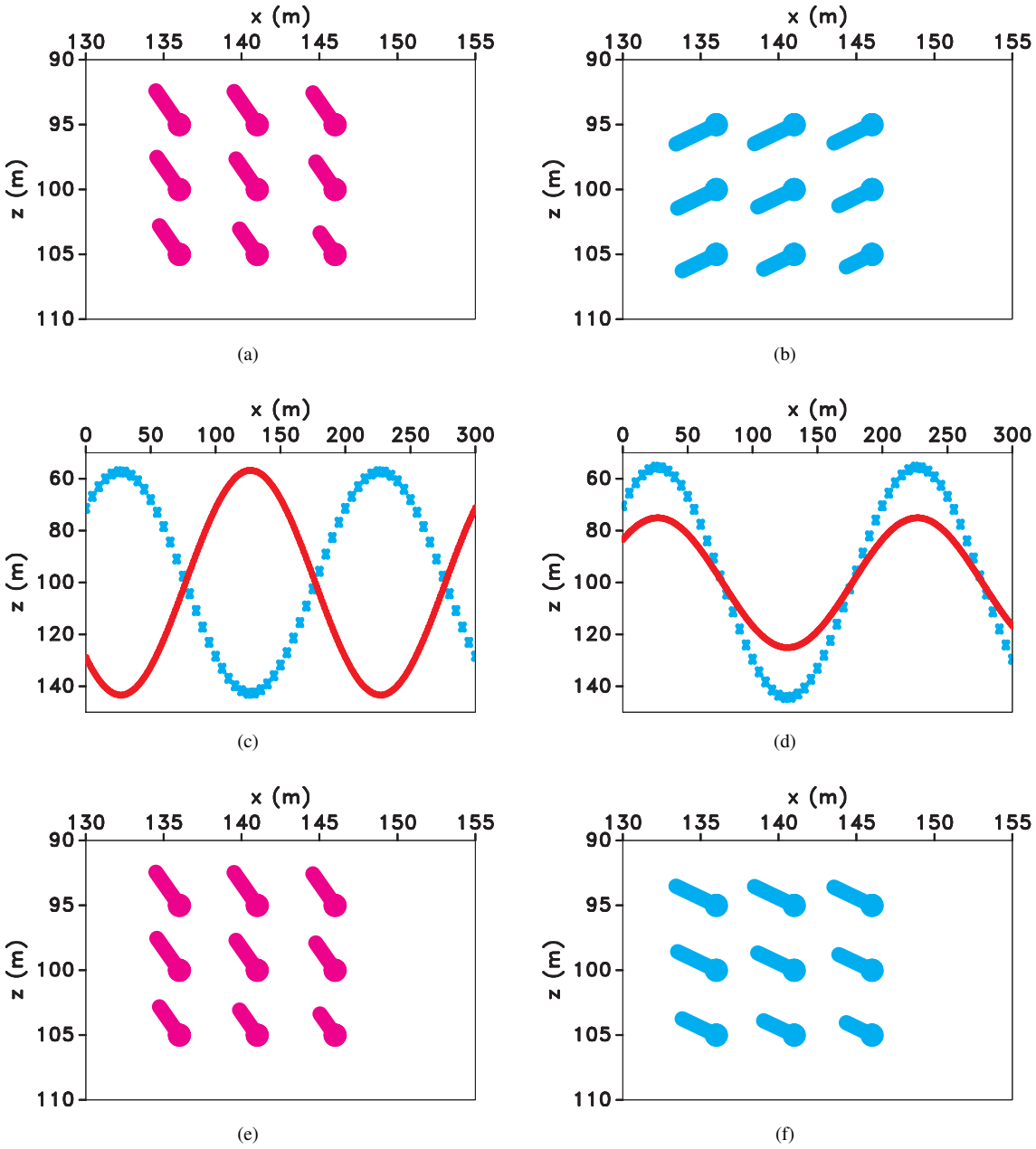


Figure 7. The analytical (a) P-wave and (b) S-wave exaggerated displacement vectors where the circles represent the vector origin. The scaled curvature (dotted line) and displacement (solid line) for (c) P-wave and (d) S-wave. The reconstructed exaggerated displacement vectors where the circles represent the vector origin for (e) P- and (f) S-waves using the calculated curvature showing the same polarization.

axial strain data and solving equation 13, we successfully reconstruct the strain field for the plane P-wave (Figure 11(b)) and the S-wave (Figure 11(d)).

To investigate the impact of the assumption that the seismic wavelength is much larger than the helix period, we perform strain tensor reconstruction for seismic wavelength equal to, twice and four times of the helix period. In this example, we use the chirping helix configuration to perform angle dependent axial strain measurements. We use the axial strain measurements along a period of the helix assuming that they refer to the same strain tensor reconstruction and compare the results with the analytic strain tensor in the middle of the helix period.

Using a helix period which is the same as the seismic wavelength shows that we are unable to reconstruct the strain field which is shown in Figure 13(a) for the observed plane

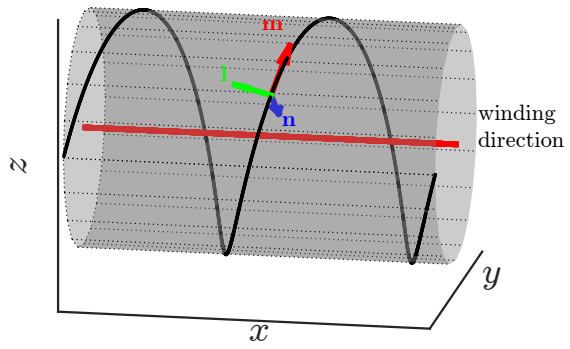


Figure 8. An example of the helical optical fiber with the associated local coordinate system.

P-wave with an incident angle of 30° and Figure 13(b) for the reconstructed strain field. This is also true for the observed plane S-wave in Figure 14(a) with an incident angle of 30° and Figure 14(b) for the reconstructed strain field. When the helix period is half of the seismic wavelength, we are able to reconstruct the strain field. However, the reconstructed strain component of ε_{xz} and ε_{zz} contains discontinuity for both P- and S-wave respectively as shown in Figure 13(c) and Figure 14(c). When the helix period is a quarter of the seismic wavelength, we successfully reduce the discontinuity in the reconstructed strain component of ε_{xz} and ε_{zz} as shown in Figure 13(d) for P-wave and Figure 14(d) for S-wave. By having the helix period at 10 times smaller than the seismic wavelength, we are able to reconstruct a strain tensor that is comparable to the observed strain tensor as shown in Figure 13(e) for P-wave and Figure 14(e) for S-wave.

We repeat the strain reconstruction using the same helix configuration and a helix period quarter of the seismic wavelength with strain tensors modeled using finite difference. The acquisition geometry is shown in Figure 15. The results in Figure 16(a) and 16(b) show successful reconstruction of the strain tensor. Using a more complex wavefield such as triplication of the wavefield due to a negative Gaussian velocity anomaly shown in Figure 17, we are able to successfully reconstruct the strain tensor shown in Figure 18(a) and 18(b).

3.2 Discussion

Our synthetic example indicates that we can reconstruct the strain tensor field if we have access to angle dependent axial strain measurements. Also, we demonstrate that the assumption of the seismic wavelength much larger than the helix period must hold for accurate strain tensor reconstruction. As seen in Figure 9(d) and 10(d), the chirping helix can provide a wider range of angles with respect to the winding direction of the traditional helix with a constant wrap angle. In 3D Figure 10(c) and 9(c) shows the traditional helix can only provide a constant angle for the axial strain measurement whereas the chirping helix can provide a range of angles due to the change in the helix frequency.

4 CONCLUSIONS

The shape sensing method applied using the parallel optical fibers is unable to accurately reconstruct correct displacements when more than one wavefield mode is involved. The reliance of this method on the gradient of the axial strain between multiple parallel optical fibers is insufficient due to lack of information to accurately reconstruct the displacement components. However, we demonstrate that the helically shaped optical fiber has the potential to obtain multicomponent DAS data. The strain tensor can be reconstructed given enough angle dependent axial strain measurements along a segment of the optical fiber which is much smaller than the seismic wavelength. This is true even for multiple wave modes as the strain tensor of the respective wave modes contributes to the axial strain along the optical fiber. Alternatives to the optical fiber helix shape allow us to measure a wider range of angle dependent axial strains compared to the traditional helix, and can reduce the possibility of redundant angle dependent measurements.

5 ACKNOWLEDGMENTS

We would like to thank the sponsors of the Center for Wave Phenomena, whose support made this research possible and Martin Karrenbach of OptaSense for fruitful discussions. The reproducible numeric examples in this paper use the Madagascar open-source software package (Fomel et al., 2013) freely available from http://www.ahay.org.

REFERENCES

Cox, B., P. Wills, D. Kiyashchenko, J. Mestayer, J. Lopez, S. Bourne, R. Lupton, G. Solano, N. Henderson, D. Hill, et al., 2012, Distributed acoustic sensing for geophysical measurement, monitoring and verification: CSEG Recorder, **37**, 7–13.

Daley, T. M., B. M. Freifeld, J. Ajo-Franklin, S. Dou, R. Pevzner, V. Shulakova, S. Kashikar, D. E. Miller, J. Goetz, J. Henninges, et al., 2013, Field testing of fiber-optic distributed acoustic sensing (DAS) for subsurface seismic monitoring: The Leading Edge, **32**, 699–706.

Davis, T. L., M. J. Terrell, R. D. Benson, R. Cardona, R. R. Kendall, and R. Winarsky, 2003, Multicomponent seismic characterization and monitoring of the CO_2 flood at Weyburn Field, Saskatchewan: The Leading Edge, **22**, 696–697.

Den, B., A. Mateeva, J. Pearce, J. Mestayer, W. Birch, J. Lopez, K. Hornman, and B. Kuvshinov, 2013, Detecting broadside acoustic signals with a fiber optical Distributed Acoustic Sensing (DAS) assembly. (WO Patent App. PCT/US2012/069,464).

Fender, A., W. MacPherson, A. Moore, J. Barton, J. Jones, S. McCulloch, B. Jones, D. Zhao, L. Zhang, and I. Bennion, 2006, Dynamic two-axis curvature measurement using multicore fiber Bragg gratings: Optical Fiber Sensors, Optical Society of America, TuE87.

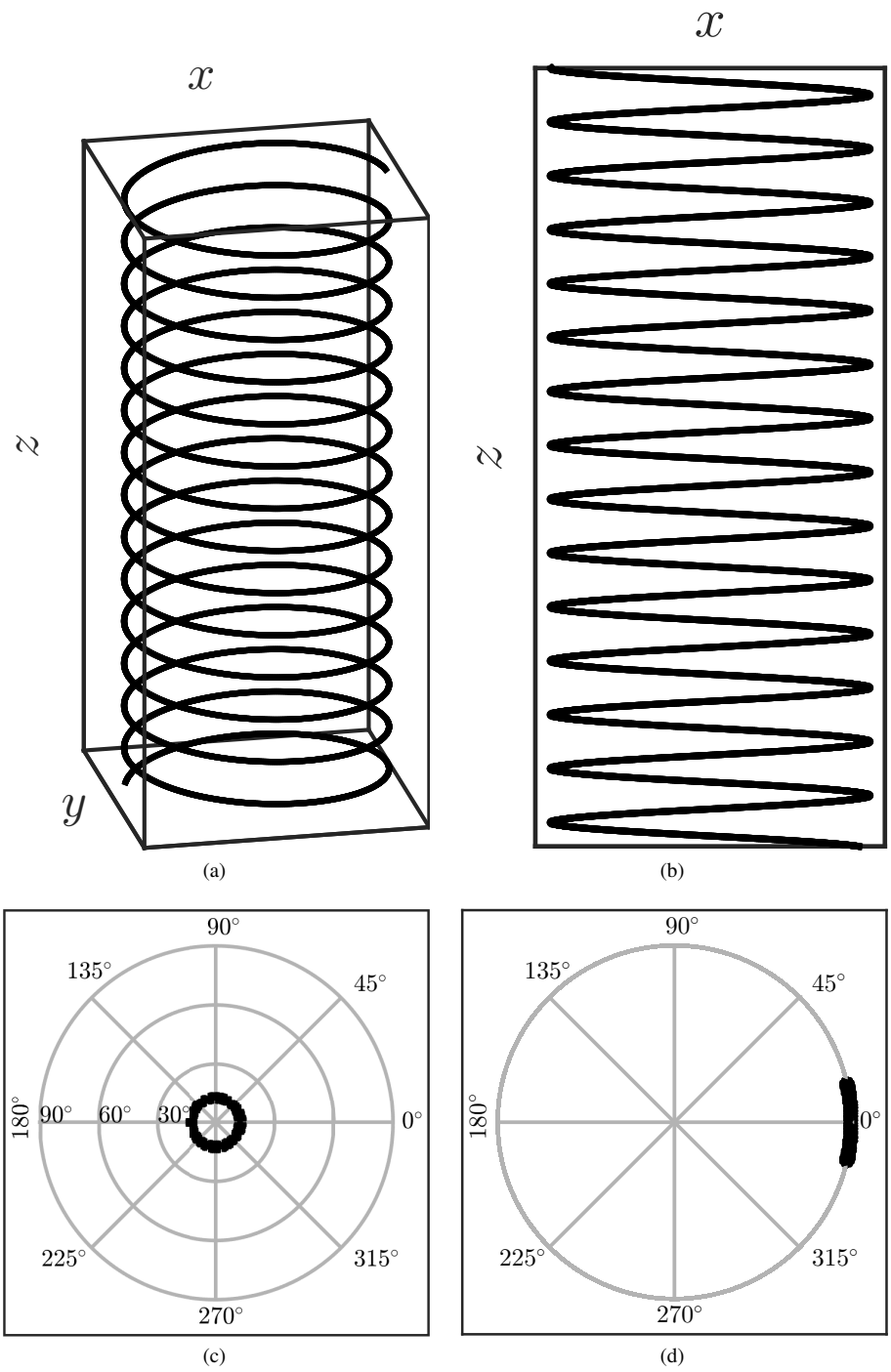


Figure 9. Example of a helical configuration for a constant wrap angle in (a) 3D and (b) 2D together with (c) the 3D projection of the local coordinate vectors of the 3D helix axial and radial directions, (d) and the 2D projection on the axial direction.

Flockhart, G., W. MacPherson, J. Barton, J. Jones, L. Zhang, and I. Bennion, 2003, Two-axis bend measurement with Bragg gratings in multicore optical fiber: Optics letters, **28**, 387–389.

Fomel, S., P. Sava, I. Vlad, Y. Liu, and V. Bashkardin, 2013, Madagascar: open-source software project for multidimensional data analysis and reproducible computational experiments: Journal of Open Research Software, **1**.

Gander, M., W. MacPherson, R. McBride, J. Jones, L. Zhang, I. Bennion, P. Blanchard, J. Burnett, and A. Greenaway,

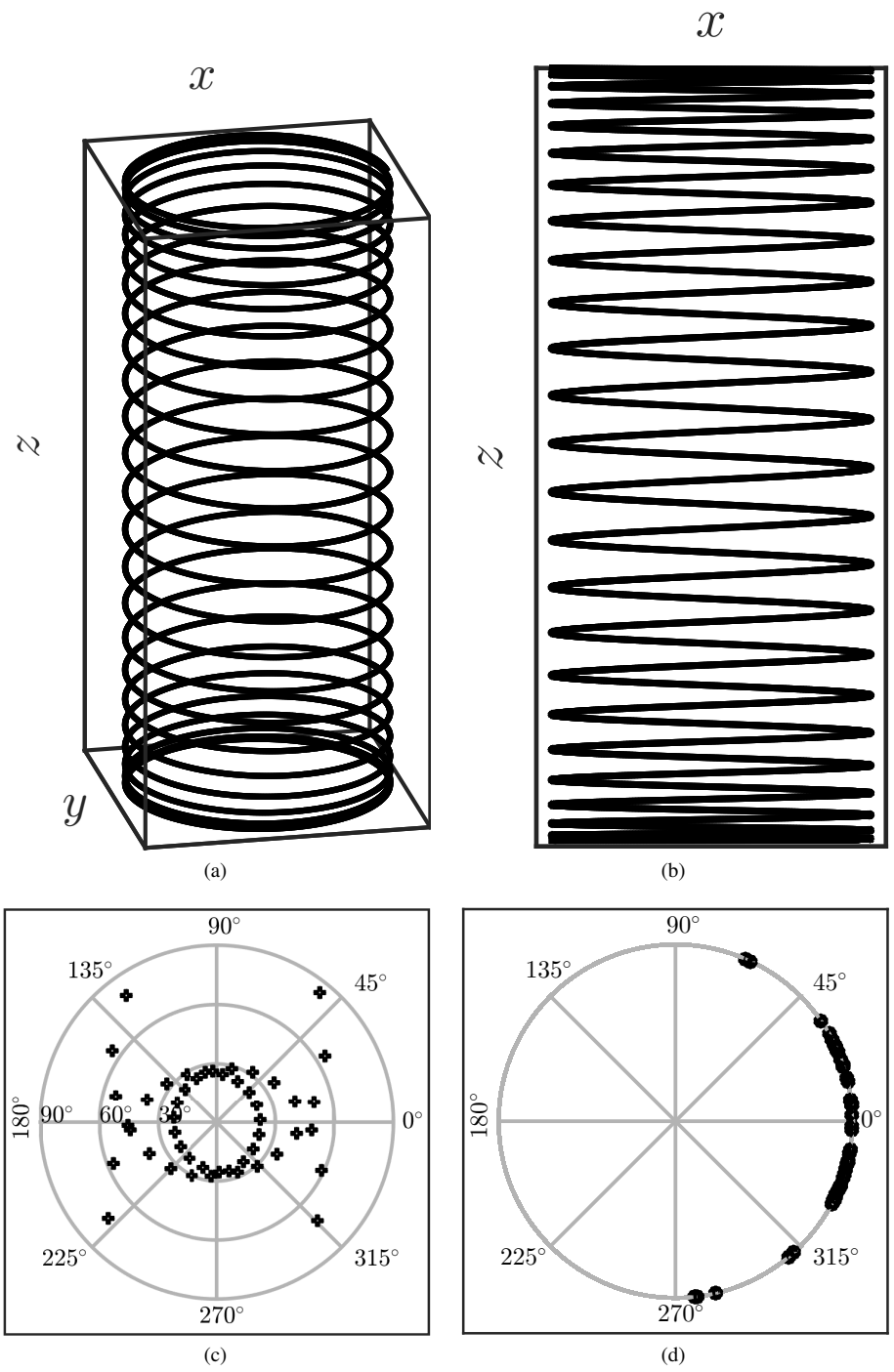


Figure 10. Example of a chirping helical configuration in (a) 3D and (b) 2D together with (c) the 3D projection of the local coordinate vectors of the 3D helix axial and radial directions, (d) and the 2D projection on the axial direction.

2000, Bend measurement using Bragg gratings in multicore fibre: Electronics Letters, **36**, 1.

Hartog, A., 2000, Distributed fiber-optic sensors: principles and applications, *in* Optical Fiber Sensor Technology: Springer, 241–301.

Karaman, O. S., R. L. Kutlik, E. L. Kluth, et al., 1996, A field trial to test fiber optic sensors for downhole temperature and pressure measurements, West Coalinga Field, California: Presented at the SPE Western Regional Meeting, Society of Petroleum Engineers.

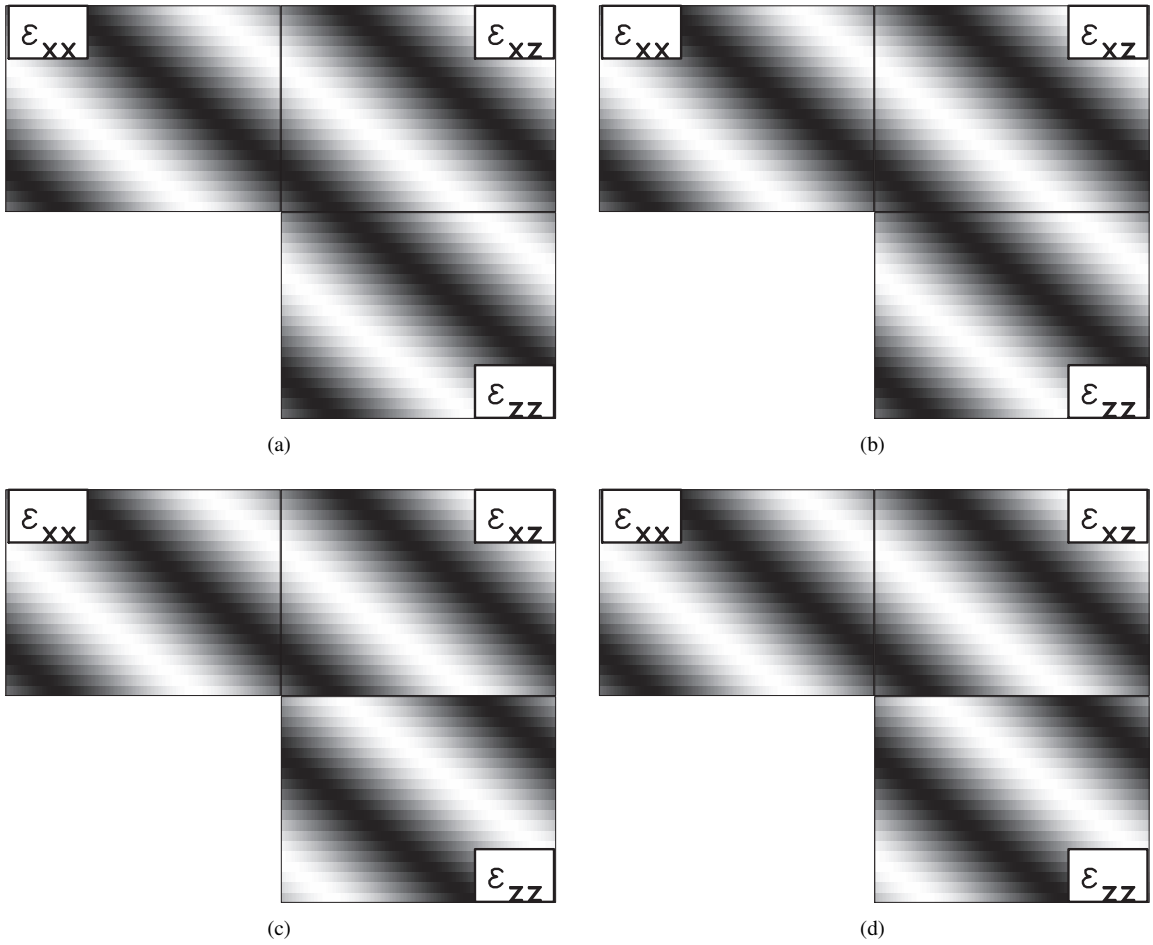


Figure 11. Strain field for plane (a) P-wave and (c) S-wave propagating at 30° with respect to the vertical axis. The reconstructed (b) P-wave and (d) S-wave by solving the least-squares inversion problem using the angle dependent axial strain measurements. For each panel, the vertical axis is time and the horizontal axis is the receiver position along the optical fiber.

Lumens, P., A. Franzen, K. Hornman, S. G. Karam, G. Hemink, B. Kuvshinov, J. La Follett, B. Wyker, and P. Zwartjes, 2013, Cable development for distributed geophysical sensing with a field trial in surface seismic: Fifth European Workshop on Optical Fibre Sensors, International Society for Optics and Photonics, 879435–879435.

Lumens, P. G. E., 2014, Fibre-optic sensing for application in oil and gas wells: Technische Universiteit Eindhoven.

Madsen, K. N., M. Thompson, T. Parker, and D. Finfer, 2013, A VSP field trial using distributed acoustic sensing in a producing well in the north sea: First Break, **31**, 51–56.

Mateeva, A., J. Lopez, J. Mestayer, P. Wills, B. Cox, D. Kiyashchenko, Z. Yang, W. Berlang, R. Detomo, and S. Grandi, 2013, Distributed acoustic sensing for reservoir monitoring with VSP: The Leading Edge, **32**, 1278–1283.

Mateeva, A., J. Mestayer, B. Cox, D. Kiyashchenko, P. Wills, J. Lopez, S. Grandi, K. Hornman, P. Lumens, A. Franzen, et al., 2012, Advances in distributed acoustic sensing (DAS) for VSP: Presented at the 2012 SEG Annual Meeting, Society of Exploration Geophysicists.

Mestayer, J., B. Cox, P. Wills, D. Kiyashchenko, J. Lopez, M. Costello, S. Bourne, G. Ugueto, R. Lupton, G. Solano, et al., 2011, Field trials of distributed acoustic sensing for geophysical monitoring: Presented at the 2011 SEG Annual Meeting, Society of Exploration Geophysicists.

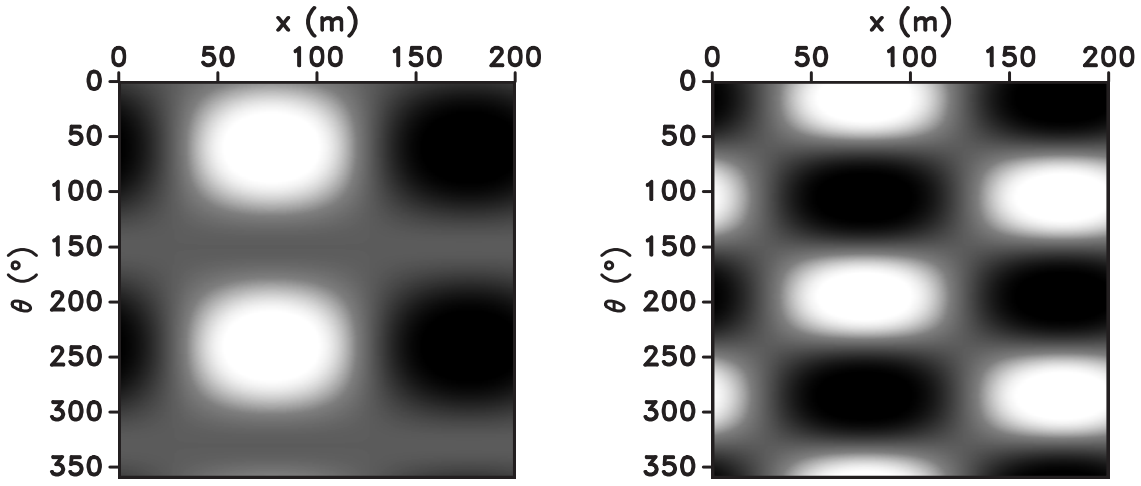
Moore, J. P., and M. D. Rogge, 2012, Shape sensing using multi-core fiber optic cable and parametric curve solutions: Optics express, **20**, 2967–2973.

Stewart, R. R., J. E. Gaiser, R. J. Brown, and D. C. Lawton, 2003, Converted-wave seismic exploration: Applications: Geophysics, **68**, 40–57.

Tsujikawa, K., K. Tajima, and J. Zhou, 2005, Intrinsic loss of optical fibers: Optical Fiber Technology, **11**, 319–331.

Uzunoglu, N. K., 1981, Scattering from inhomogeneities inside a fiber waveguide: JOSA, **71**, 259–273.

Young, W. C., and R. G. Budynas, 2002, Roark's formulas for stress and strain: McGraw-Hill New York, **7**.



(a) (b)

Figure 12. Time snapshot of the axial strain of optical fiber for plane (a) P-wave and (b) S-wave with a wavelength of 100m as a function of angles θ between the orientation of the optical fiber and the axial direction. The differences between the axial strain for P- and S-waves that allow for the reconstruction of the respective strain tensor without ambiguity.

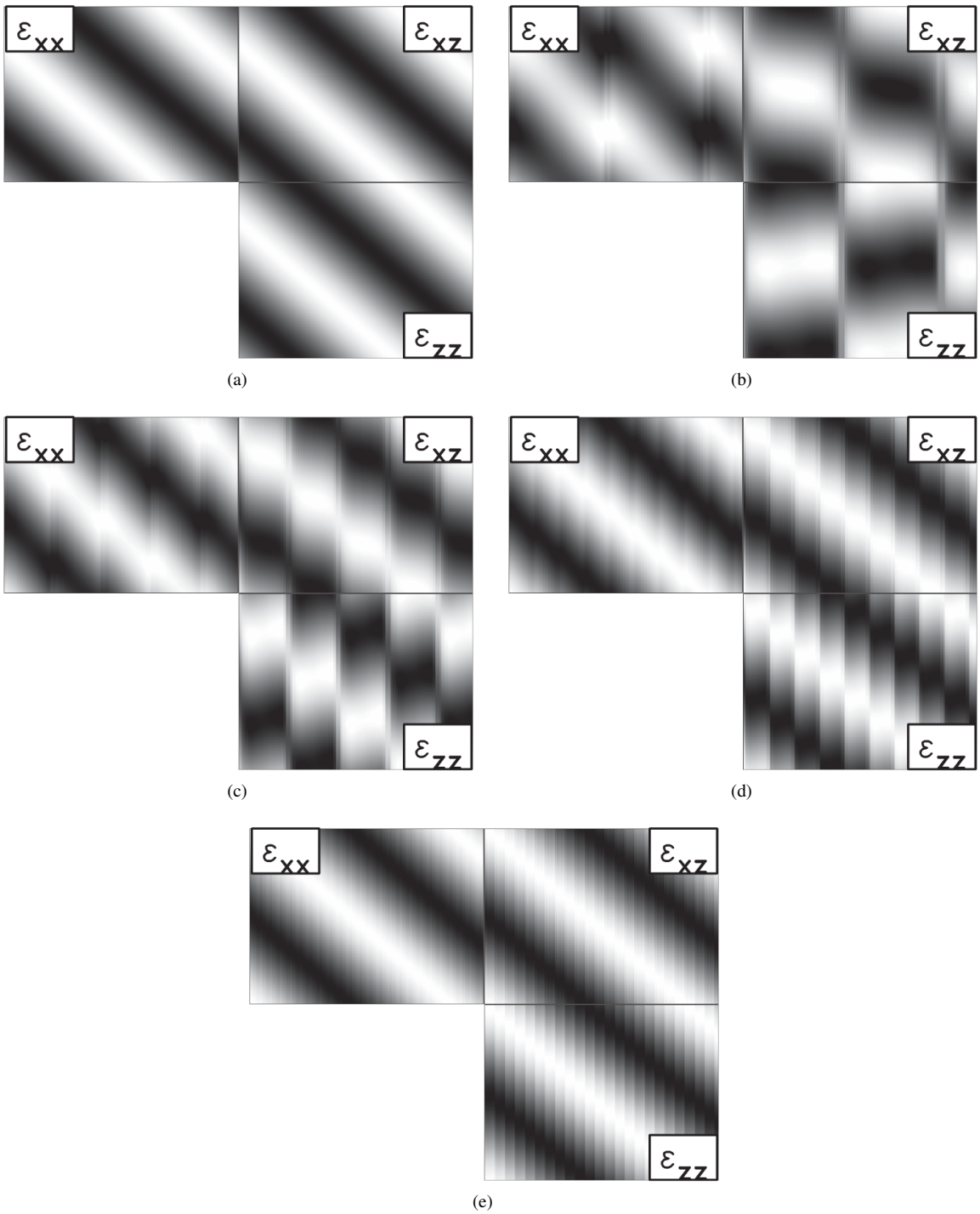


Figure 13. The panels show a plane P-wave propagating with a 30° angle of incidence with respect to the vertical axis. We show comparisons between the (a) analytical tensor and reconstructed strain tensor using a helix period (b) equal to, (c) 2 times, (d) 4 times, and (e) 10 times smaller than the seismic wavelength. The discontinuity observed in the strain component of ε_{xz} and ε_{zz} reduces with the helix period.

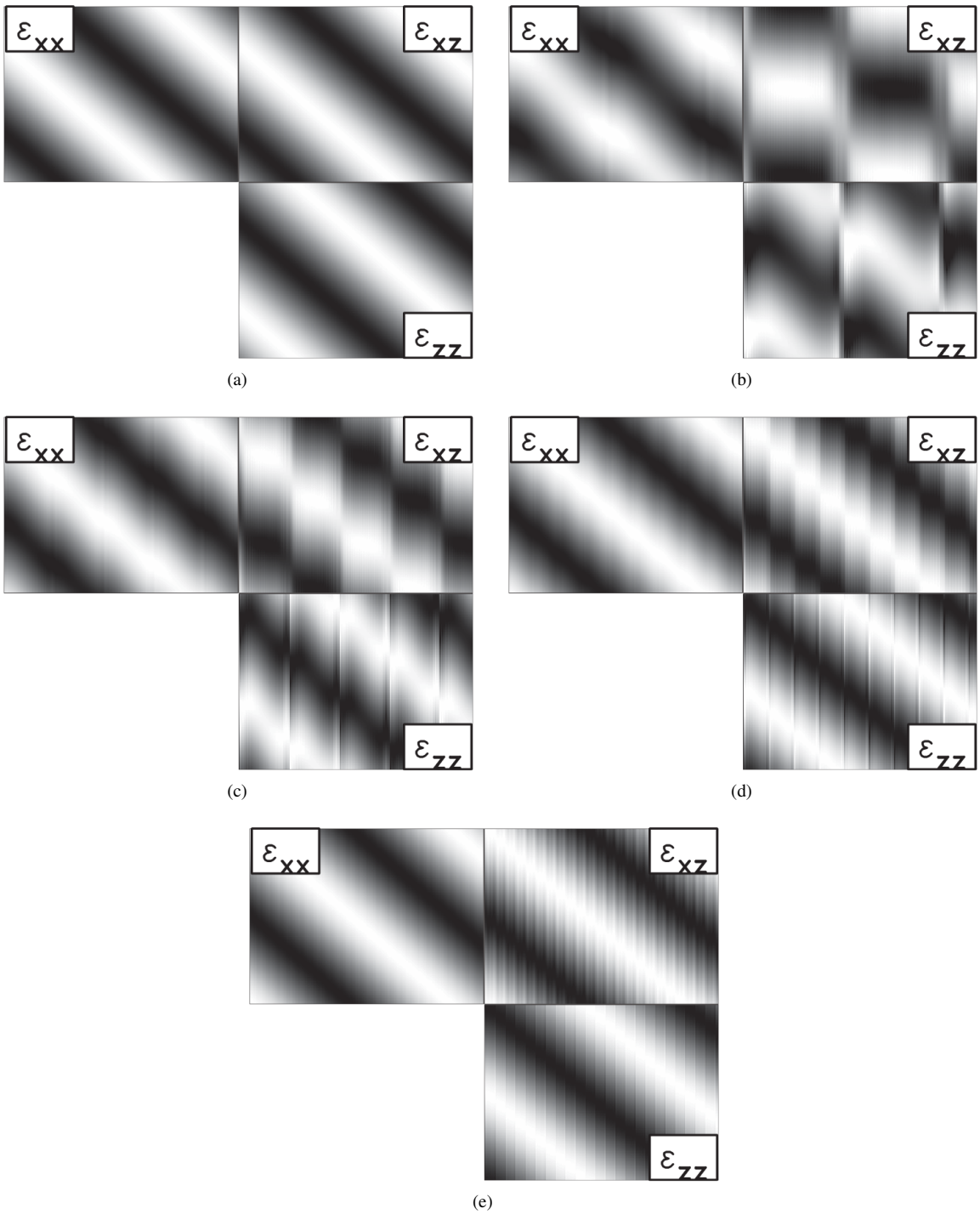


Figure 14. The panels show a plane S-wave propagating with a 30° angle of incidence with respect to the vertical axis. We show comparisons between the (a) analytical tensor and reconstructed strain tensor using a helix period (b) equal to, (c) 2 times, (d) 4 times, and (e) 10 times smaller than the seismic wavelength. The discontinuity observed in the strain component of ε_{xz} and ε_{zz} reduces with the helix period.

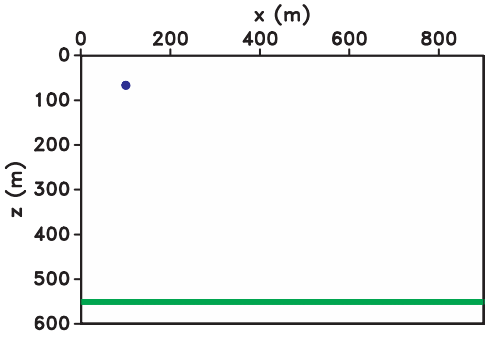


Figure 15. Source (dot) and receiver (horizontal line) position for the finite difference strain tensor modeling overlay on a constant velocity model.

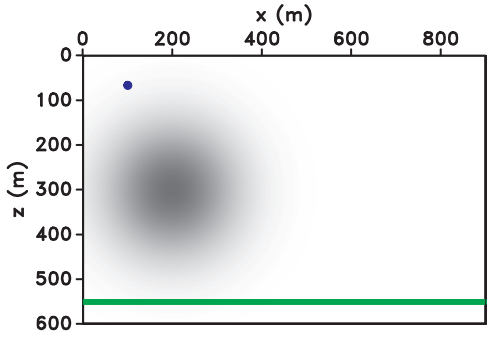


Figure 17. Source (dot) and receiver (horizontal line) position for the finite difference strain tensor modeling overlay on a velocity model with a negative Gaussian anomaly.

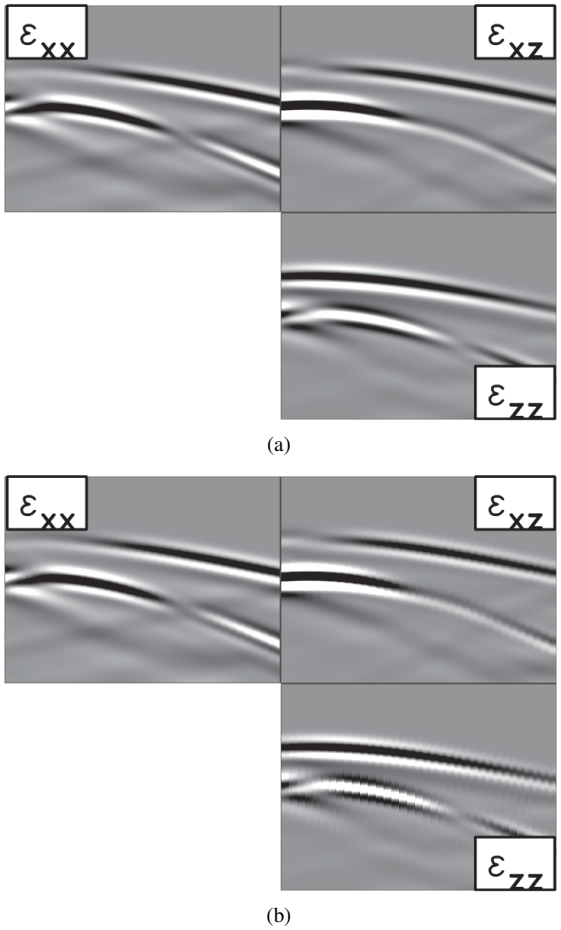


Figure 16. (a) Strain tensor obtained by forward simulation using the geometry from the model in Figure 15 and (b) strain tensor reconstructed reconstructed using chirping helical optical fiber with the geometry from Figure 10(a).

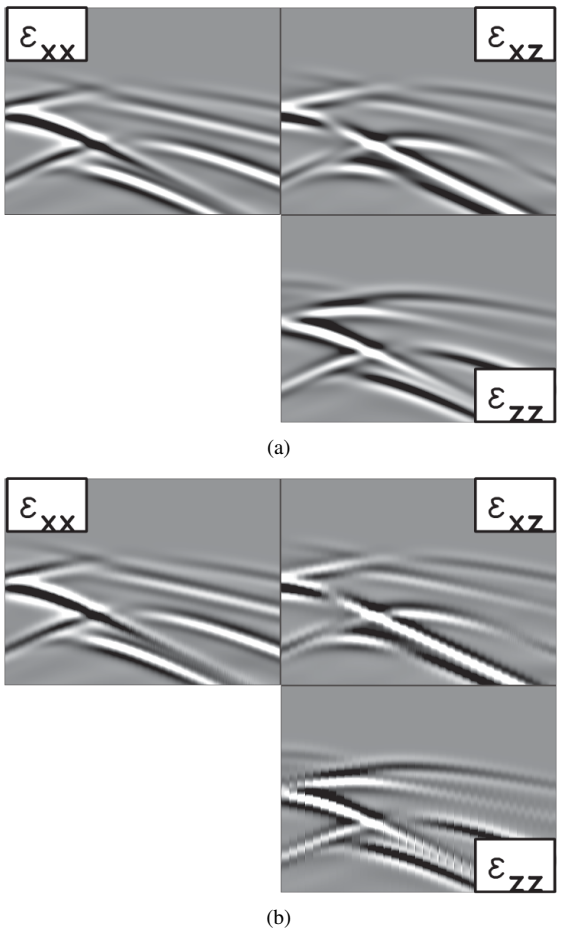


Figure 18. (a) Strain tensor obtained by forward simulation using the geometry from the model in Figure 17 and (b) strain tensor reconstructed reconstructed using chirping helical optical fiber with the geometry from Figure 10(a).